ORGANIC CHEMISTRY FRONTIERS

RESEARCH ARTICLE

View Article Online
View Journal | View Issue

Cite this: *Org. Chem. Front.*, 2026, **13**, 2794

Reaction profiling of visible-light-mediated [2 + 1] dearomatization *vs.* alkylation of electron-rich arenes with aryldiazoacetates: real-time NMR monitoring, kinetics, and computational analysis

Karlo Petrić, [a] Ana Čikoš, [b] Ivana Nikšić-Franjić, [a] Guy C. Lloyd-Jones, *[c] Matija Gredičak *[a] and Nikola Topolovčan *[a]

Received 19th January 2026,
Accepted 6th March 2026

DOI: 10.1039/d6qo00072j

rsc.li/frontiers-organic

An in-depth mechanistic and kinetic analysis of the dearomative [2 + 1] reaction between electron-rich arenes and aryldiazoesters for the regioselective and diastereoselective synthesis of norcaradienes is reported. Profiling the reaction through LED-NMR analysis gave kinetic insights into product formation and unwanted side reactions, and the influence of the electron-density profile on cyclopropanation *vs.* alkylation in the key dearomative step is elucidated by theoretical analysis. Synthetic utility of the obtained *meso*-norcaradienes was evaluated through their desymmetrization into products with six contiguous stereogenic centres, while reactive functional groups allow for subsequent manipulation into more complex carbocycles.

Introduction

The concept of dearomatization has progressively emerged as a key approach in organic synthesis, as it represents a straightforward conversion of abundant aromatic feedstock into higher-order carbocycles without the need for laborious functional group interconversions. In addition to already well-established protocols, the employment of visible light has emerged as a reliable tool with applications in various dearomatization reactions.[1,2]

Recent findings on the photolysis of donor–acceptor aryldiazoacetates under blue light irradiation, resulting in the formation of highly reactive carbenes, have unlocked their synthetic potential in cheletropic reactions with a range of trapping agents.[3] The distinct photochemical behaviour of donor–acceptor aryldiazoacetates has already been substantially exploited, and the current corpus of work has given a strong momentum for further exploratory studies.[4–7] The notable ability of photogenerated carbenes to undergo dearomative [2 + 1] cycloaddition with aromatic and heteroaromatic systems has prompted focused investigations into the extent of this transformation.[8] The outcome of carbene transfer reactions with indoles or benzenes under blue light irradiation strongly depends on the nucleophilicity of the aromatic ring. In the case of indoles, depleted electron density at the C-3 position attained by installing an electron-withdrawing group on the nitrogen atom results in cyclopropanation. At the same time, the C-3-alkylated product is formed with the more electron-rich *N*-methylated indole (Scheme 1a).[9,10] A similar trend was also observed in benzene and its derivatives, where electron-rich arenes, used as solvents, were transformed into the alkylation products,[11] while a substantial effect of electron-neutral functionality reflected on the preferred dearomatization over the alkylation process (Scheme 1b and c).[12]

Access to norcaradienes through carbene transfer onto benzenes enables rapid build-up of molecular complexity, making this process a platform for the introduction of other functional groups.[13–18] In the context of this work, it is also important to mention that the complementary transition-metal-catalyzed carbene insertion is effective in transforming simple aromatic starting compounds into more complex molecules.[19–21] However, while these types of dearomatizations are synthetically valuable, the lack of a detailed correlation between the chemoselectivity and electron distribution in electronically distinct arenes hampers the exploitation of their full synthetic potential. Thus, with this work, we offer a comprehensive profiling of the competitive dearomatization/alkylation processes, intending to shine a light on the factors behind the observed reactivity (Scheme 1d).

In addition, from the synthetic perspective and within the framework of known findings on the photochemically induced synthesis of norcaradienes and their subsequent transformation, we have identified several areas where further progress

[a]*Division of Organic Chemistry and Biochemistry, Ruđer Bošković Institute, Bijenička cesta 54, 10 000 Zagreb, Croatia. E-mail: ntopolov@irb.hr*
[b]*NMR Centre, Ruđer Bošković Institute, Bijenička cesta 54, 10 000 Zagreb, Croatia*
[c]*School of Chemistry, University of Edinburgh, Edinburgh EH9 3FJ, UK*

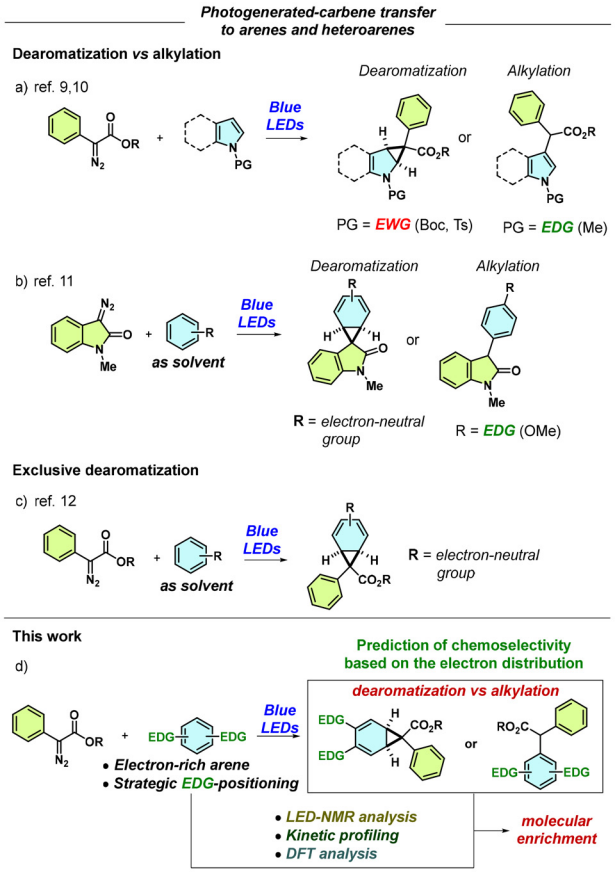

Scheme 1 Relevant visible light-mediated dearomatizations and our work.

could be made (Fig. 1). The main issues to be addressed are (i) reducing the excess of arene required for dearomative cyclopropanation, (ii) dearomatization of arenes with embedded transformable functional groups, (iii) dearomatization of electron-rich arenes by suppressing undesired alkylation, and (iv) further structural build-up of the formed norcaradienes enabled by the presence of transformable functionality. Present challenges are reflections of current limitations, and bridging the gap between the inability to dearomatize electron-rich arenes and the dormant chemical potential of diversely functionalized norcaradienes would contribute to this rapidly expanding field.

Since competitive alkylation in indoles could be suppressed by tuning the electronic nature of the C2–C3 bond, we envisioned that a similar strategy might be translated to benzene derivatives as well. An electron-donating functional group in benzene imprints its mesomeric effect by increasing the nucleophilicity of *ortho*- and *para*-positioned carbon atoms, which serve as attachment points for photogenerated carbenes, thus resulting in alkylation products (Fig. 2a). We envisioned that the vicinal placement of an isoelectronic or electronically similar group would exhibit a cancelling effect by suppressing the nucleophilicity of α and β positions (Fig. 2b). In this way, the overall electron distribution would resemble that of electron-neutral benzene with three distinct cyclopropanation sites that might give three different regioisomers, most probably the one with the least steric hindrance.

With a focus on elucidating the factors that govern the dearomatization process over the parasitic alkylation side reaction, we herein report a visible-light-mediated cyclopropanation of electron-rich arenes with concomitant molecular decoration, enabled by the chemistry of functional groups responsible for increased electron density. The overall synthetic design consists of sequential (i) dearomatization through cyclopropanation, (ii) construction of σ-bishomobenzenes, and (iii) cyclopropane-ring opening (Scheme 2).

The selection of an appropriate electron-rich arene is critical since the functional group on the arene has to fulfil several conditions. First of all, it has to significantly contribute to the alteration of the electron density of the aromatic ring compared to unsubstituted benzene, thus making it prone to competitive alkylation. Second, it has to be inert to reaction with aryldiazoacetates and with *in situ*-formed carbenes, and finally, it has to possess transformable ability that would allow subsequent modification. Free phenols and alcohols in general, together with anilines, are excluded from the available aromatic substrate pool because of their ability to undergo O–H and N–H functionalizations with photogenerated carbenes.[22–26] On the other hand, aryl–alkyl ethers should meet the required criteria, and a considerable amount of poss-

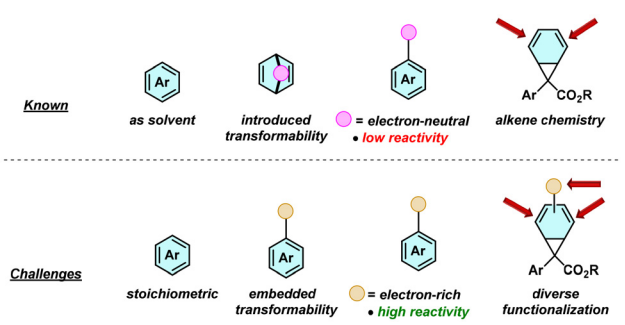

Fig. 1 Limitations and challenges of visible light-mediated dearomatization of arenes.

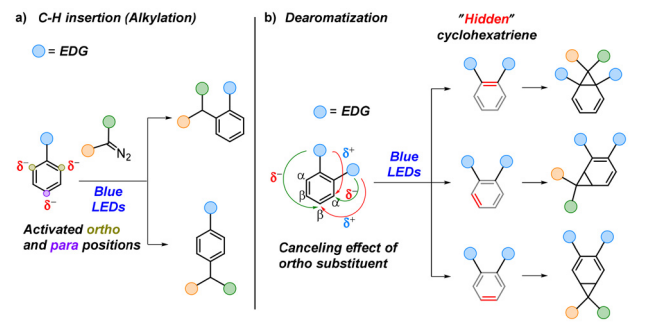

Fig. 2 (a) Alkylation *vs.* (b) dearomatization governed by the electronic nature of arenes.

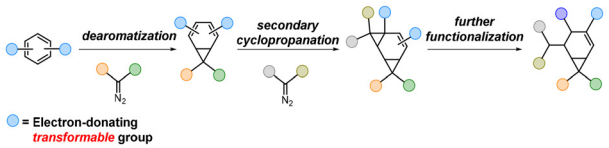

Scheme 2 Dearomative approach toward functionalized carbocycles.

ible variations obtained through transposition of functional groups around the aromatic ring would allow studies on the correlation between the electron-donating ability and the positioning of the functional group on the reaction outcome.

Results and discussion

Guided by previous conditions used for dearomatization of benzenes, we started our investigation using 1,2-dimethoxybenzene **2a** as a model substrate, and the initial reaction with methyl 2-diazo-2-phenylacetate **1a** afforded the norcaradiene **3aa**. A high level of regio- and diastereoselectivity was accompanied by rather low efficiency of the dearomatization process under the used reaction conditions. In order to increase the yield of the cyclopropanated product, reaction parameters such as solvent, concentration, reaction time, and the ratio between reagents were selectively changed, and a maximum of 36% isolated yield was achieved (for screening of reaction conditions see the SI).

The rather low yield of the norcaradiene **3aa** can be attributed to the formation of a considerable amount of side products isolated from the reaction mixtures (Fig. 3). The dearomatization event leading to norcaradiene **3aa** is followed by two reactions that directly diminish its yield: the secondary cyclopropanation resulting in σ-bishomobenzene **4aa** and the formation of cyclohexatriene **5**. On the other hand, the high reactivity of *in situ*-formed carbenes is evident through the formation of

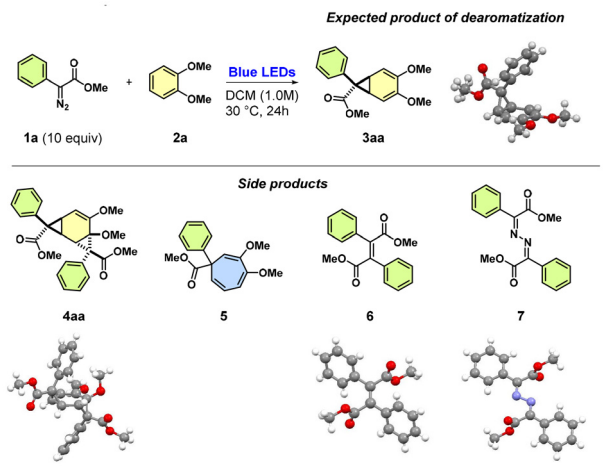

Fig. 3 Products formed in the reaction between the aryldiazoester **1a** and 1,2-dimethoxybenzene **2a**, and their crystal structures.

dimer **6**, the formal product of the reaction between two carbene molecules. Azine **7** is formed when the *in situ*-generated carbene reacts with the starting aryldiazoester **2a**. It is evident that the side-reaction of the limiting reagent, together with the consumption of the formed norcaradiene, substantially affects the overall efficiency of the dearomatization process. It should be noted that all side products were isolated and confirmed by single-crystal X-ray analysis, except for product **5**, which was confirmed by 2D NMR analysis.[27]

The formation of side products **6** and **7** is a general issue in the reactions of diazoacetates, as unstabilized carbenes are highly reactive, thereby interfering with the effectiveness of the desired transformation.[28–31] Although Koenigs showed that this issue could be lessened by generating diazoesters through the Bamford–Stevens reaction of tosyl hydrazones,[10] determining the timeline of formation for each of the formed products would provide more insight into how to either minimize or completely suppress undesired side-product formation in favor of the dearomatization process. For this purpose, we monitored *in situ* the progress of the reaction using LED-NMR, where the sample was irradiated with a blue LED lamp at 470 nm, with continuous measurement of ^{1}H NMR spectra. The consumption of the aryldiazoacetate **1a** is accompanied by the generation of dearomatized products **3aa**, **4aa**, and **5**, along with the carbene side products **6** and **7**. Continuous *in situ* NMR analysis avoids the possibility of mechanistic ambiguities arising from product interconversion during isolation (Fig. 4a). In addition, the on–off experiments (Fig. 4b) exclude the interference from any significant background reactions, thus indicating direct or indirect light-dependent formation of all products. We also compared the reactivity of the norcaradiene **3aa** and 1,2-dimethoxybenzene **2a** in the presence of aryldiazoacetate **1a** (Fig. 4c). The rate of reaction of **2a** is significantly lower than that of **3aa**, which is converted to σ-bishomobenzene **4aa**. Kinetic simulations (see later) indicate that **3aa** is five-fold more reactive than **2a** toward the carbene intermediate. We were thus intrigued by why the formation of products of type **4aa** had not previously been reported in the literature during the dearomatization of benzene and its derivatives. We hypothesized that the presence of the methoxy groups activates the double bonds in **3aa** for secondary cyclopropanation. To test this, we prepared the known norcaradiene **3aa-deOMe** and compared its reactivity with **3aa** under standard reaction conditions, using 1.0 equivalent of the carbene precursor **1a** (Fig. 4d). Kinetic simulations, *vide infra*, of the reaction progress monitored by LED-NMR showed that the norcaradiene **3aa** is four-fold more reactive than **3aa-deOMe** toward the carbene intermediate, resulting in σ-bishomobenzene **4aa** being generated in excess over **4aa-deOMe**.

The temporal concentration data from the *in situ* LED-NMR monitoring were analyzed by kinetic simulations using a sequential partitioning model.[32,33] In this model, the 470 nm emission from the LED passes through the reaction mixture in the NMR tube at a constant light intensity ($L = E\ \mathrm{M}^{-1}\ \mathrm{s}^{-1}$) with a fraction, f_1, being absorbed by the diazo chromophore in **1a** with Beer–Lambert behaviour, [**1a**]εl. The resulting excited

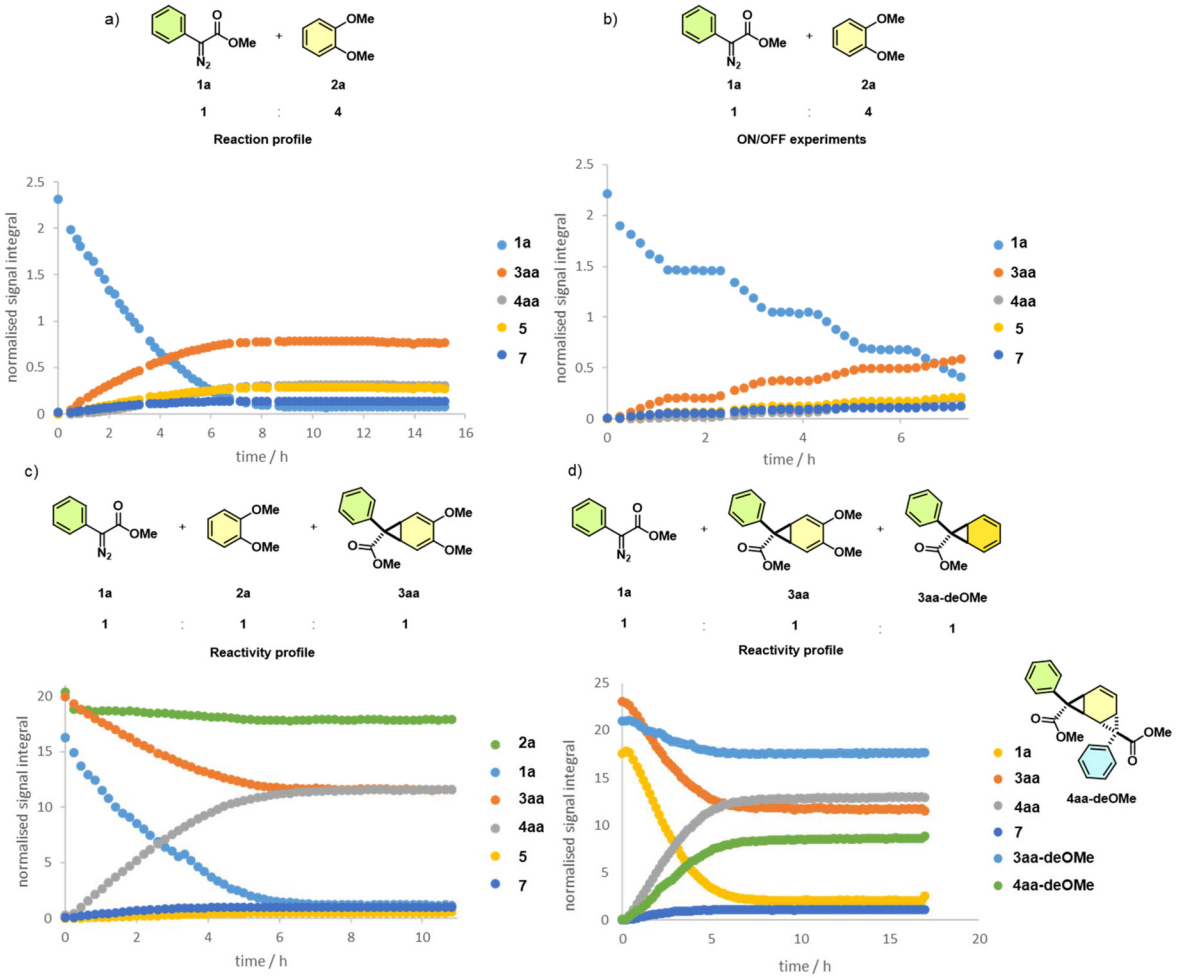

Fig. 4 LED-NMR experiments. Continuous light irradiation at 470 nm, in methylene chloride-d_2, at 25 °C was used in all reactions. (a) Reaction profile of the reaction between **1a** and **2a** showing product formation, (b) ON/OFF experiments for the reaction between **1a** and **2a**, (c) comparison of reactivity between **1a**, **2a** and **3aa**, and (d) comparison of reactivity between **1a**, **3aa** and **3aa-deOMe**.

state, **1a***, either undergoes relaxation $(1 - q)$ or fragments (q) to generate N_2 and the carbene. The nascent carbene is captured by **2a**, **3aa**, and **1a** to generate **3aa**, **4aa**, **5**, **6**, and **7**, and steady-state conditions are attained. The temporal evolution of the system can then be predicted based on the rate of carbene generation, Lf_1q, and five partitioning factors, f_2, f_3, f_4, f_5, and f_6. Nonlinear regression of the variables against the experimental data gives a satisfactory correlation (Fig. 5; see the SI for full details). The sigmoidal profile for the generation of **4aa** confirms that it is dependent on the development of the less reactive precursor **3aa**. Conversely, the non-sigmoidal profile for **5** shows that it is generated directly from **2a** and not *via* rearrangement of **3aa**.

The LED-NMR and kinetic simulations, Fig. 4 and 5, lead to four main conclusions that can rationalize the effectiveness of the dearomatization reaction of 1,2-dimethoxybenzene **2a**: (i) the consumption of starting materials and the formation of all side products is a simultaneous process, (ii) the products are formed exclusively under irradiation with blue light, (iii) the product of dearomatization (norcaradiene) is more reactive than the arene from which it was obtained, and (iv) the cycloheptatriene ('Buchner') product **5** is generated directly from **2a**, *i.e.*, not *via* a photo- or thermally induced rearrangement of the norcaradiene **3aa**. These key mechanistic insights show that suppressing the four simultaneous side reactions in favour of the norcaradiene is challenging. The extent of this limitation in terms of the aromatic substrate was explored (Scheme 3), focusing on the possibility of further modification of the norcaradiene through the presence of transformable functional groups. Exchange of one methoxy group for the easily removable MOM protection group afforded norcaradiene product **3ba** in modest yield, since the dearomatization reaction was again accompanied by the formation of several side products. Moving from a 1,2- to a 1,3-disubstitution pattern induced a large change in the reactivity of the arene, with only the alkylation products **8da** and **8ea** isolated. The same reactivity was expressed in the trisubstituted arene, where again, prevalent substitution took place over the dearomatization,

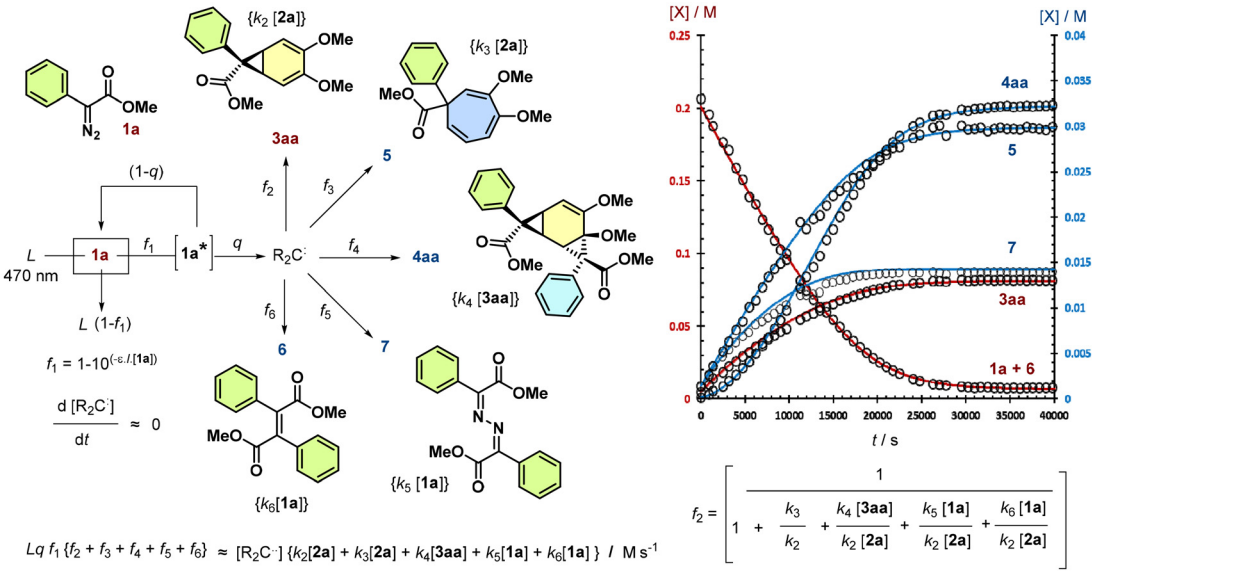

Fig. 5 Partitioning model[32,33] for the kinetics of the light-mediated reaction of **1a** with **2a**, evolving after an initial period during which steady-state conditions are attained, together with an example of the model (solid lines) and experimental data (open circles) acquired by LED-^{1}H-NMR. The model was fitted by temporal evolution (Euler, Δt = 10 s, 5000 steps) minimising the SSE against four experimental datasets and iteration of the six fitting coefficients. In the example shown, $L(q)$ = 1.0 × 10^{-5} M s^{-1}, εl = 11 M^{-1}, k_3/k_2 = 0.26, k_4/k_2 = 5.27, k_5/k_2 = 1.05, and k_6/k_2 = 0.24. For full details and further examples, see the SI.

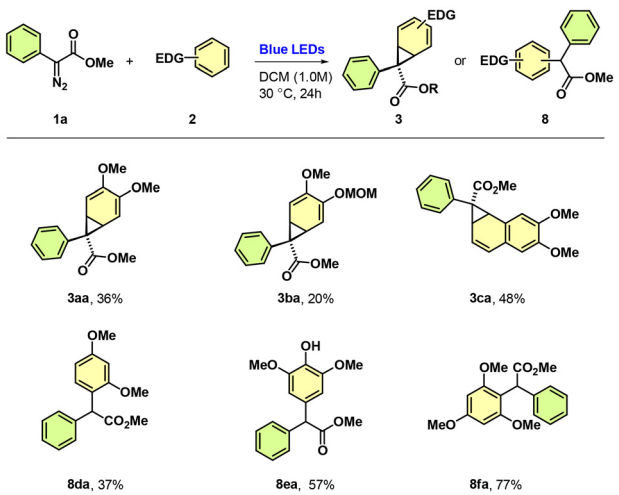

Scheme 3 Substrate scope – arenes.

leading to **8fa**. On the other hand, in the case of 2,3-dimethoxynaphthalene, the cyclopropanation occurred at the distal aromatic ring, affording the dearomatization product **3ca** in a rather satisfactory isolated yield, considering the overall effectiveness of the reaction. Similar products were previously prepared using 10.0 equivalents of polycyclic arenes.[12] Comparing the obtained yields, it appears that the reaction between highly electron-rich arenes, leading to alkylation products, as exemplified by 1,3,5-trimethoxybenzene, is much faster than the dearomatization processes, where the simultaneous formation of several side products is allowed.

The observed reactivity can be attributed to the electronic profile of the substituted electron-rich arenes. In the case of 1,2-disubstituted arenes, regioselective cyclopropanation at only one of the possible reactive sites is most probably a consequence of similar local atomic charge distribution between two neighbouring carbon atoms on which transformation occurs. On the other hand, if the atomic charge distribution between neighbouring atoms is substantial, then the alkylation products are formed. The regioselectivity of the studied substrates is fundamentally governed by the underlying electronic distribution, as evidenced by the high correlation between Mulliken (**M**), Natural Bond Orbital – NBO (**N**), and Hirshfeld (**H**) charges. For substrate **2a**, the three charge schemes consistently show a symmetric electronic environment at the reactive centers; the Mulliken charges (≈−0.285), the NBO charges (−0.237), and the Hirshfeld charges (−0.069) are identical for atoms C4 and C5 (Fig. 6). This electronic equivalence is further supported by the ESP map of **2a**, which displays a uniform negative potential (red zone) distributed across the C4–C5 bond, facilitating exclusive cyclopropanation. In contrast, **2d** exhibits a sharp electronic polarization characterized by a significant disparity in partial atomic charges between the reactive centers. The most pronounced differences are observed between C4/C6 and C5, with NBO charges of −0.343 *vs.* −0.177 and Hirshfeld charges of −0.088 *vs.* −0.047, respectively. The ESP map for **2d** confirms this electronic asymmetry, revealing localized nucleophilic 'hotspots' at the C4/C6 positions. This marked differentiation in the electronic environment across the aromatic ring prioritizes site-specific interaction at these positions, providing a clear rationale for the prevalence of alkylation over dearomatization in this

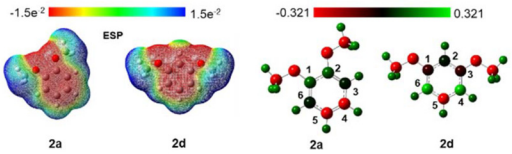

Atom	Charge	1	2	3	4	5	6
2a	M	0.114	0.114	0.031	**-0.285**	**-0.286**	0.031
	N	0.293	0.293	-0.300	**-0.237**	**-0.237**	-0.300
	H	0.048	0.048	-0.074	**-0.069**	**-0.069**	-0.074
2d	M	-0.069	0.028	-0.069	**0.219**	**-0.615**	**0.219**
	N	0.347	-0.319	0.347	**-0.343**	**-0.177**	**-0.343**
	H	0.062	-0.092	-0.092	**-0.088**	**-0.047**	**-0.088**

Fig. 6 Electrostatic potential map (ESP), charge distribution, Mulliken partial atomic charges (**M**), natural bond orbital (**N**), and Hirshfeld charges (**H**) of 1,2-dimethoxybenzene **2a** and 1,3-dimethoxybenzene **2d** at the M06-2X-D3/6-311+G(2d,p) level of theory in dichloromethane (SMD solvent model).

isomer. This is supported by the fact that in all other cases (**8ea** and **8fa**), alkylation occurs at the most available or most nucleophilic sites, meaning that there is a substantial impact of the electron density distribution on the reaction outcome.

Furthermore, the Fukui index analysis provides a deeper predictive basis for the experimental regioselectivity (Fig. 7). For 1,2-dimethoxybenzene **2a**, the symmetric distribution of $f(+)$ and $f(-)$ indices across C4 and C5 facilitates exclusive cyclopropanation. Conversely, for 1,3-dimethoxybenzene **2d**, the indices are significantly larger at C4/C6 relative to C5. This electronic localization prioritizes site-specific alkylation and explains the shift in reactivity compared to the 1,2-substituted isomer.

To further rationalize the selectivity of the cyclopropanation reaction of **2a**, we studied the dearomatization reaction by DFT calculations at the M06-2X-D3/6-311+G(2d,p) (solvent = dichloromethane) level of theory (Fig. 8). We initiated our calculations with the free singlet carbene, which can undergo a cyclopropanation reaction with **2a** occurring at positions 4 and 5, which are equivalent due to symmetry reasons, and also the Mulliken partial atomic charges are basically identical at these positions. Also, at the same level of theory, the triplet state of

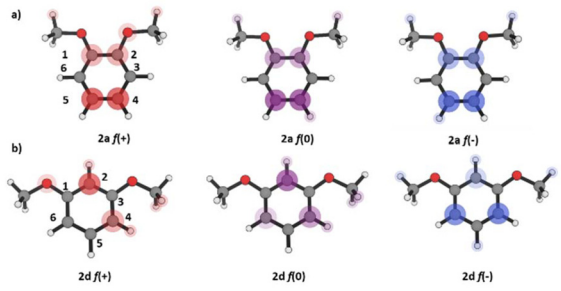

Fig. 7 Graphical representation of the positive, zero, and negative Fukui indices of **2a** and **2d** calculated at the M06-2X/6-31++G(d) level of theory in dichloromethane (PCM solvation model).

the methyl 2-phenylacetate carbene was calculated. The results show that the triplet state is more stable than the singlet state by a narrow margin of 0.96 kcal mol^{-1}. While this small energy gap falls within the typical range of computational error, the triplet pathway was ruled out based on thermodynamic feasibility. Specifically, the formation of the observed products **3aa** and **8da** from the triplet carbene is calculated to be significantly endergonic, with Gibbs free energies of 20.02 kcal mol^{-1} and 12.16 kcal mol^{-1}, respectively. These values indicate that the triplet pathway is inconsistent with the experimental results.

Furthermore, the involvement of a free singlet carbene as the active species is consistent with previous studies on closely related chemical systems, such as the photochemical cyclopropanation of cyclooctatetraene and other (poly)unsaturated carbocycles reported by Koenigs and co-workers. Consequently, the singlet carbene pathway was used as the basis for the transition-state analysis and mechanistic discussions presented in this study.

We could identify two possible transition-state structures because of the different "anti-parallel" (TS1-**2a**) and "parallel" (TS2-**2a**) orientations of aromatic rings. According to the reaction profile, TS2-**2a** with a parallel orientation of benzene rings has a 4.93 kcal mol^{-1} lower reaction barrier than TS1-**2a** with an anti-parallel orientation. This difference in Gibbs free energy accounts for the observed high stereoselectivity, and aromatic stacking interactions play a crucial role, which renders TS2-**2a** more favourable than TS1-**2a**. Both transition states are reactant-like with C–C distances in the range of 2.3–2.7 Å, while intermediates and products end with the formation of one or two C–C bond(s), d = 1.5 Å. Interpolation of the reaction paths between INT1-**2a**/INT2-**2a** and products **3aa′**/**3aa** enabled us to locate the ring-closing transition states TS3-**2a** and TS4-**2a**, respectively, although their energies are very similar to those of the preceding intermediates. Moreover, the energy difference between these two transition states is less than 2 kcal mol^{-1}, while on the other hand, **3aa** product formation is more favourable by 5.85 kcal mol^{-1} compared to **3aa′**.

In addition, the 2D NCI (non-covalent interaction) isosurfaces provide a clear spatial representation of the stabilization differences between the two transition states (TS1-**2a** and TS2-**2a**), leading to two different diastereoisomers. A significantly larger and more continuous green isosurface is observed between the aromatic rings of the reactants in TS2-**2a** (Fig. 9). This indicates superior spatial overlap of the π–π systems, facilitating extensive non-covalent stabilization that effectively lowers the transition-state energy. In contrast, the NCI surface for TS1-**2a** appears smaller and more fragmented. This suggests that the reactants in this orientation are either poorly aligned or further apart, resulting in weaker dispersion-based stabilization and a consequently higher activation barrier. While the global profiles of the RDG (reduced density gradient) plots for both transition states show similar features, a detailed examination of the "spikes" reveals the quantitative advantage of TS2-**2a**. In the van der Waals region (green zone,

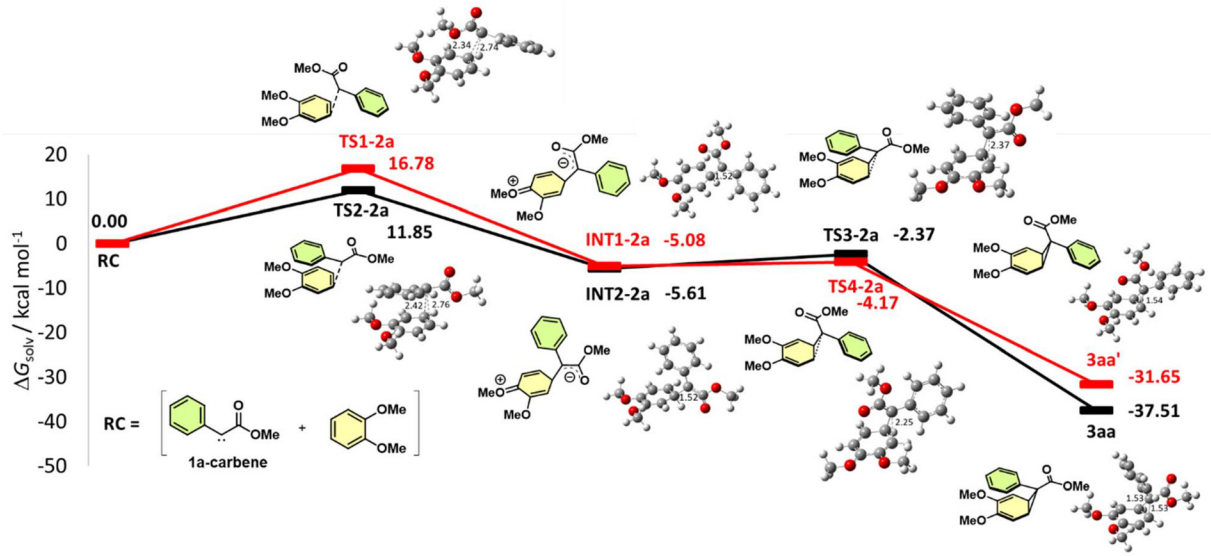

Fig. 8 Reaction profile of the cyclopropanation of **2a** and relevant structures: RC – reactant complex, TS – transition states, INT – intermediates (distances in Å), calculated at the M06-2X-D3/6-311+G(2d,p) level of theory in dichloromethane (SMD solvent model).

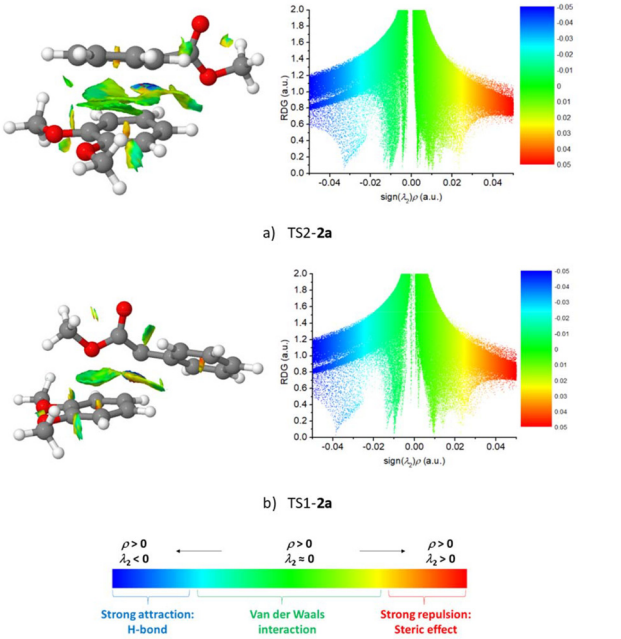

Fig. 9 Non-covalent interaction (NCI) analysis of the competing transition states, (a) TS2-**2a** (favourable) and (b) TS1-**2a** (unfavourable). (Left) NCI isosurfaces (isovalue = 0.5 a.u.) and (right) reduced density gradient (RDG) scatter plots. The blue–green–red color scale indicates the nature of the interactions, ranging from strong attraction to strong repulsion.

sign(λ_2)$\rho \approx 0$), TS2-**2a** exhibits a denser population of points that descend closer to the *X*-axis (RDG values <0.2). This confirms that the non-covalent stabilization in TS2-**2a** is more localized and energetically significant. The "attractive" region of the plot (cyan/green transition, $-0.02 <$ sign(λ_2)$\rho < -0.01$ a.u.) shows more pronounced and better-defined spikes for TS2-**2a**. These spikes serve as a direct electronic signature of the attractive π–π stacking interactions that stabilize the TS2-**2a** geometry over TS1-**2a**. Both structures show similar spikes in the repulsive region (red/yellow zone, +0.01 to +0.02 a.u.), suggesting that the difference in their relative stability is primarily driven by the magnitude of attractive dispersion forces rather than a significant difference in steric hindrance.

To clarify more deeply the preferential formation of the **3aa** product, we evaluated the HOMO and LUMO orbitals of the TS structures and products, as shown in Fig. 10. The relevant orbitals have π-character, but a larger orbital overlap can be observed in both TS2-**2a** and **3aa**, stressing once more the importance of aromatic π–π stacking interactions in stabilizing transition-state structures and reaction products.

We next probed the reaction of 1,3-dimethoxybenzene **2d** and the methyl 2-phenylacetate carbene to explain the formation of the substitution product on the C4/C6 atom. Initially, the addition of the carbene across the aromatic ring proceeds through TS1-**2d**. As shown in Fig. 11, the reaction barrier is 10.97 kcal mol^{-1}, slightly lower than that for **2a**, and the transition state is also an "early" one (relevant C–C distance of 2.48 Å), leading to the dearomatized intermediate INT1-**2d**. Then, the intramolecular protonation of the ester group in INT1-**2d** proceeds *via* TS2-**2d**, a proton-transfer transition state characterized by a relatively high harmonic vibrational frequency (≈−500 cm^{-1}) for this reaction mode. In TS2-**2d**, the partially negatively charged oxygen atom of the ester group abstracts a hydrogen atom from the cyclohexadiene moiety, leading to the aromatized intermediate INT2-**2d**, which contains the ester group in its enol form. For the transformation between INT2-**2d** and the final product, we located a

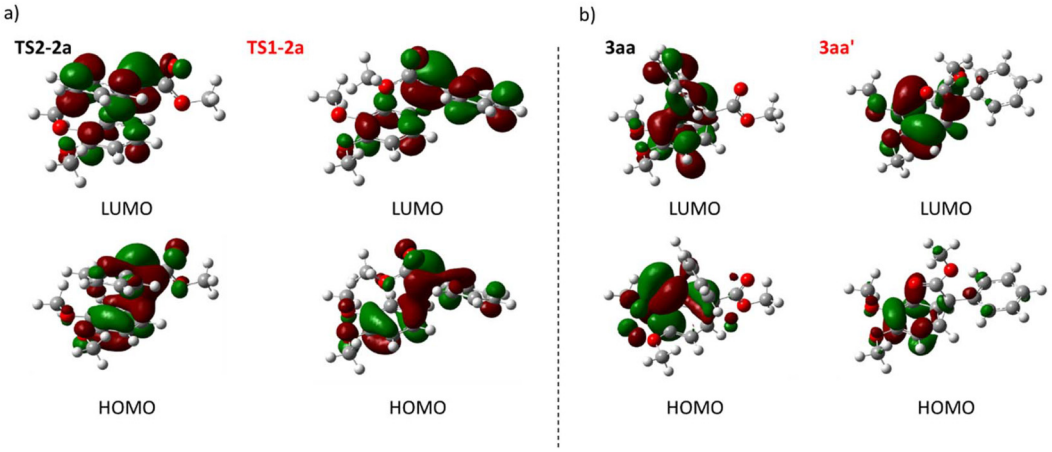

Fig. 10 HOMO and LUMO orbitals of the (a) TS structures and (b) reaction products of cyclopropanation of **2a**, calculated at the M06-2X-D3/6-311+G(2d,p) level of theory in dichloromethane (SMD solvent model); isovalue = 0.03, density = 0.0004.

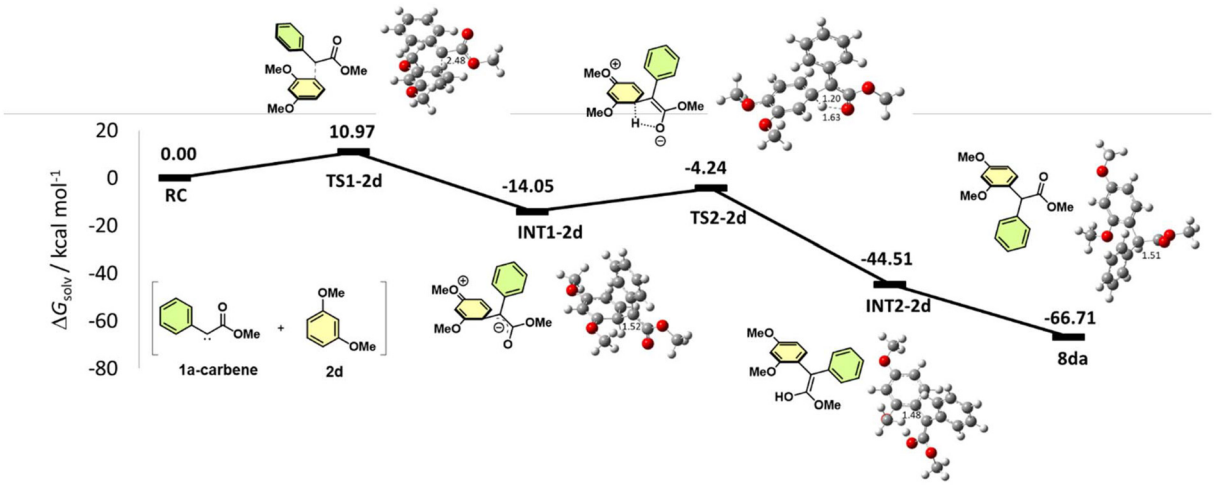

Fig. 11 Reaction profile of alkylation of 1,3-dimethoxybenzene **2d** and relevant structures: RC – reactant complex, TS – transition states, INT – intermediates (distances in Å), calculated at the M06-2X-D3/6-311+G(2d,p) level of theory in dichloromethane (SMD solvent model).

higher-order saddle point characterized by several imaginary vibrational modes (not shown in the energy profile). One of these modes corresponds to C–H bond formation. The formation of the substitution product at the C4 atom is highly exergonic (−66.71 kcal mol^{-1}), almost double that of the cyclopropanation product **3aa**. This supports the fact that for 1,3-dimethoxybenzene **2d**, there is no competition between cyclopropanation and aromatic substitution products, and only the substitution product **8da** is formed.

Since the dearomatization is limited to 1,2-disubstituted electron-rich arenes, we continued our investigation by screening the effect of electronic and structural changes in aryldiazoesters on the efficiency of the dearomatization process. Changing the position and electronic properties of the substituent on the aromatic ring of aryldiazoesters had only a marginal effect on the yield of the reaction, and norcaradienes **3aa–3ae** were isolated in comparable yields. Similar reactivity was exhibited by replacing the methyl ester with ethyl and isopropyl esters in diazoacetates that gave the dearomatization products **3ag** and **3ah**. Slightly better performance was observed with the benzyl ester that afforded the norcaradienes **3i** and **3j** in 45% and 36% isolated yields, respectively (Scheme 4). It should be noted that all norcaradienes were obtained with a >20 : 1 diastereoisomeric ratio.

The σ-bishomobenzene **4aa**, isolated as a side product, has interesting structural features that could be exploited in the construction of advanced intermediates towards more complex cyclohexanes. Thus, the high reactivity of the norcaradiene **3aa** formed in the subsequent cyclopropanation prompted us to explore the extent of this transformation (Scheme 5). The addition of various aryldiazoesters onto norcaradiene **3aa** afforded a series of σ-bishomobenzenes **4aa–4ji** with isolated yields in the range of 53–89%. Despite the full consumption of the starting norcaradiene, the low yields in some cases can be

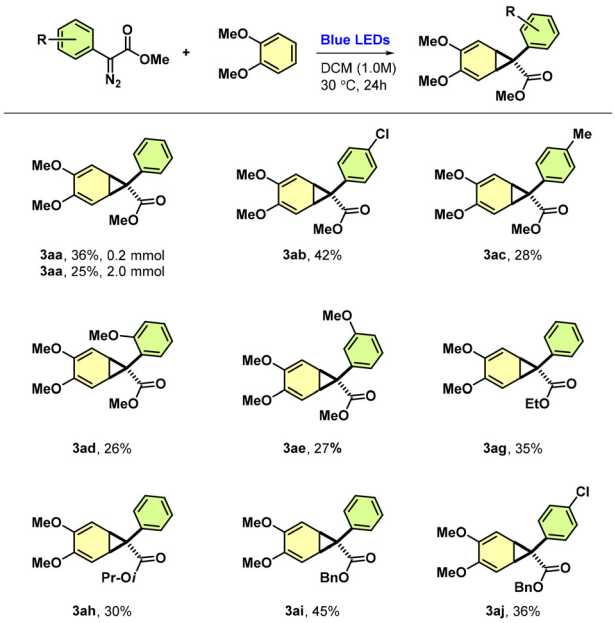

Scheme 4 Substrate scope – aryldiazoesters.

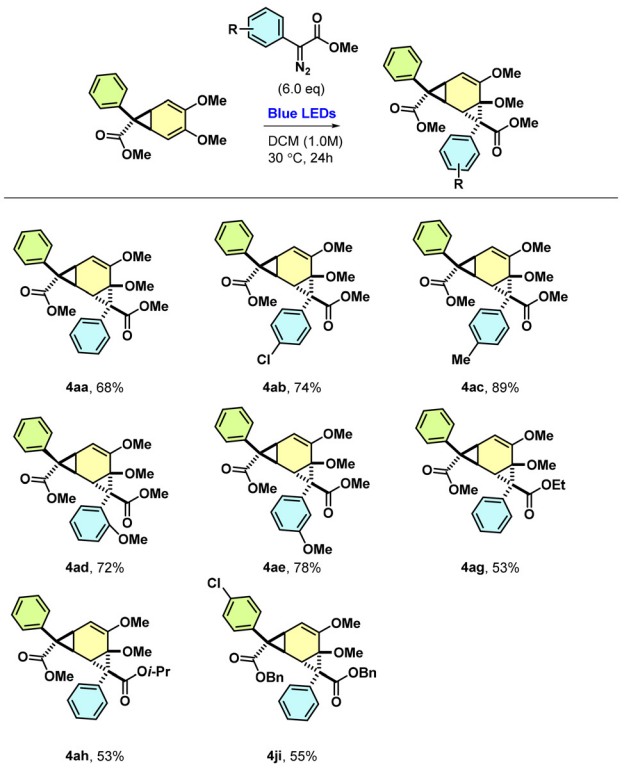

Scheme 5 Cyclopropanation of norcaradienes **3**.

attributed to the difficulties in isolating the products from several side products. The stereoselective approach of the carbene to either of the two double bonds can proceed only from the opposite side of the phenyl ring in **3aa**, which results in high diastereoselectivity. In addition, secondary cyclopropanation

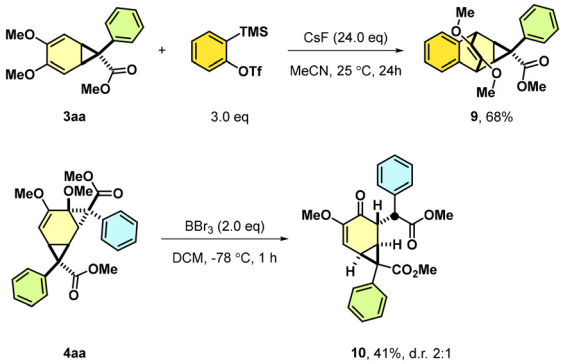

Scheme 6 Transformations of formed products.

affords compounds with six contiguous centers of chirality, of which two are quaternary and one is tetrasubstituted.

The product utility of the formed norcaradienes was exemplified in the reaction of **3aa** with *in situ*-generated benzyne (Scheme 6). The reaction cleanly resulted in the Diels–Alder adduct **9**. The 2D NMR analysis confirmed the formation of the expected *exo*-product, whose formation is a consequence of the stereochemistry of the starting norcaradiene **3aa**. Finally, the retained transformability of the formed σ-homobenzene bearing two ether functionalities that originate from the starting dearomatized arene allows further build-up of molecular complexity. A standard demethylation protocol applied to **4aa** resulted in chemoselective deprotection of just one methoxy ether with simultaneous cyclopropane ring opening that afforded enone **10** in a 2 : 1 diastereoisomeric ratio.

Conclusion

In conclusion, we profiled the reaction between electron-rich arenes and aryldiazoacetates through LED-NMR analysis, which provided kinetic insights into product formation and unwanted side reactions, while DFT calculations explained how the uneven electron-density distribution of differently substituted electron-rich arenes affects the dearomatization *vs.* alkylation processes. The synthetic utility of the norcaradienes possessing activated double bonds was exemplified in building more complex tricyclic structures bearing six contiguous centres of chirality. The presence of a transformable unit in σ-bishomobenzene allowed subsequent molecular decoration, thus showcasing their synthetic potential.

Author contributions

K. P. and N. T. conducted the photochemical experiments. A. Č. conducted the LED-NMR experiments. I. N.-F. performed the computational analysis. G. C. L.-J. carried out the kinetics simulations. M. G. acquired funding. N. T. conceived the project and oversaw the

experimental work. All authors contributed to the writing of the manuscript and the SI.

Conflicts of interest

There are no conflicts to declare.

Data availability

The data supporting this work are included in the supplementary information (SI). Supplementary information: experimental procedures, details and compound characterization, NMR analysis and NMR spectra, crystallographic data, computational data and kinetic modeling. See DOI: **https://doi.org/10.1039/d6qo00072j**.

CCDC 2487752 and 2488064–2488066 (**3aa**, **6**, **7** and **4aa**) contain the supplementary crystallographic data for this paper.[27a–d]

Acknowledgements

Financial support was provided by the Croatian Science Foundation (grant no. IP-2022-10-5184). The authors thank Dr Krunoslav Užarević and Dr Katarina Lisac (Division of Physical Chemistry, RBI) for the IR measurements and Dr Branka Bilić (Division of Physical Chemistry, RBI) for the HRMS measurements.

References

1 Z. Y. Xu, X. T. Gu, Y. Wei and M. Shi, Visible-Light-Mediated Intramolecular Dearomatization of Naphthalene and Anthracene with Bicyclo[1.1.0]butanes Through Energy Transfer Catalysis, *Angew. Chem., Int. Ed.*, 2025, **64**, e202506073.
2 Y. Z. Cheng, Z. Feng, X. Zhang and S. L. You, Visible-light induced dearomatization reactions, *Chem. Soc. Rev.*, 2022, **51**, 2145–2170.
3 I. D. Jurberg and H. M. L. Davies, Blue light-promoted photolysis of Aryldiazoacetates, *Chem. Sci.*, 2018, **9**, 5112–5118.
4 C. Empel, C. Pei and R. M. Koenigs, Unlocking novel reaction pathways of diazoalkanes with visible light, *Chem. Commun.*, 2022, **58**, 2788–2798.
5 Ł. W. Ciszewski, K. Rybicka-Jasińska and D. Gryko, Recent developments in photochemical reactions of diazo compounds, *Org. Biomol. Chem.*, 2019, **17**, 432–448.
6 Z. Yang, M. L. Stivanin, I. D. Jurberg and R. M. Koenigs, Visible light- promoted reactions with diazo compounds: a mild and practical strategy towards free carbene intermediates, *Chem. Soc. Rev.*, 2020, **49**, 6833–6847.
7 J. Durka, J. Turkowska and D. Gryko, Lightening Diazo Compounds?, *ACS Sustainable Chem. Eng.*, 2021, **9**, 8895–8918.
8 Z. Zhang and V. Gevorgyan, Visible Light-Induced Reactions of Diazo Compounds and Their Precursors, *Chem. Rev.*, 2024, **124**, 7214–7261.
9 X. Zhang, C. Du, H. Zhang, X. C. Li, Y. L. Wang, J. L. Niu and M. P. Song, Metal-Free Blue-Light-Mediated Cyclopropanation of Indoles by Aryl(diazo)acetates, *Synthesis*, 2019, 889–898.
10 S. Jana, F. Li, C. Empel, D. Verspeek, P. Aseeva and R. M. Koenigs, Stoichiometric photochemical carbene transfer reactions via Bamford Stevens reaction, *Chem. – Eur. J.*, 2020, **26**, 2586–2591.
11 S. Zhao, X. X. Chen, N. Gao, M. Qian and X. Chen, Visible-Light-Mediated Cyclopropanation Reactions of 3-Diazooxindoles with Arenes, *J. Org. Chem.*, 2021, **86**, 7131–7140.
12 Y. Guo, T. V. Nguyen and R. M. Koenigs, Norcaradiene Synthesis via Visible-Light-Mediated Cyclopropanation Reactions of Arenes, *Org. Lett.*, 2019, **21**, 8814–8818.
13 E. T. Crawford, K. L. Smith and J. S. Johnson, Dearomative Synthesis of Chiral Dienes Enables Improved Late-Stage Ligand Diversification, *Org. Lett.*, 2022, **24**, 1791–1795.
14 S. M. Wilkerson-Hill, B. E. Haines, D. G. Musaev and H. M. L. Davies, Synthesis of [3a,7a]-Dihydroindoles by a Tandem Arene Cyclopropanation/3,5-Sigmatropic Rearrangement Reaction, *J. Org. Chem.*, 2018, **83**, 7939–7949.
15 H. M. Mbuvi and K. L. Woo, Addition of carbenes derived from aryldiazoacetates to arenes using chloro(tetraphenylporphyrinato)iron as catalyst, *J. Porphyrins Phthalocyanines*, 2009, **13**, 136–152.
16 K. L. Smith, C. L. Padgett, W. D. Mackay and J. S. Johnson, Catalytic, Asymmetric Dearomative Synthesis of Complex Cyclohexanes via a Highly Regio- and Stereoselective Arene Cyclopropanation Using α-Cyanodiazoacetates, *J. Am. Chem. Soc.*, 2020, **142**, 6449–6455.
17 W. D. MacKay and J. S. Johnson, Kinetic Separation and Asymmetric Reactions of Norcaradiene Cycloadducts: Facilitated Access via H_2O-Accelerated Cycloaddition, *Org. Lett.*, 2016, **18**, 536–539.
18 M. Yang, T. R. Webb and P. Livant, High-Yield Double Cyclopropanation of Benzene, *J. Org. Chem.*, 2001, **66**, 4945–4949.
19 D. Chen, Y. Zhou, C. H. Tung, Z. X. Yu and Z. Xu, A Desymmetric Dearomatization Cyclopropanation of [2.2] Paracyclophane, *CCS Chem.*, 2025, **7**, 1509–1521.
20 F. Guan, R. Zhou, X. Ren, Z. Guo, C. Wang and C. Y. Zhou, Asymmetric dearomative cyclopropanation of naphthalenes to construct polycyclic compounds, *Chem. Sci.*, 2022, **51**, 13015–13019.
21 M. Liu and C. Uyeda, Redox Approaches to Carbene Generation in Catalytic Cyclopropanation Reactions, *Angew. Chem., Int. Ed.*, 2024, **63**, e202406218.
22 Q. Li, B. G. Cai, L. Li and J. Xuan, Oxime Ether Synthesis through O–H Functionalization of Oximes with Diazo Esters under Blue LED Irradiation, *Org. Lett.*, 2021, **23**, 6951–6955.
23 S. Zhou, B. Cai, C. Hu, X. Cheng, L. Li and J. Xuan, Visible light and base promoted O-H insertion/cyclization of para-

quinone methides with aryl diazoacetates: An approach to 2,3-dihydrobenzofuran derivatives, *Chin. Chem. Lett.*, 2021, **32**, 2577–2581.

24 C. Pei and R. M. Koenigs, A Computational Study on the Photochemical O–H Functionalization of Alcohols with Diazoacetates, *J. Org. Chem.*, 2022, **87**, 6832–6837.

25 S. Jana, Z. Yang, F. Li, C. Empel, J. Ho and R. M. Koenigs, Photoinduced proton transfer reactions for mild O-H functionalization reactions of unreactive alcohols, *Angew. Chem., Int. Ed.*, 2020, **59**, 5562–5566.

26 C. Empel, S. Jana, C. Pei, T. V. Nguyen and R. M. Koenigs, Photochemical O–H Functionalization of Aryldiazoacetates with Phenols via Proton Transfer, *Org. Lett.*, 2020, **22**, 7225–7229.

27 (*a*) CCDC 2487752: Experimental Crystal Structure Determination, 2026, DOI: **10.5517/ccdc.csd.cc2phq20**; (*b*) CCDC 2488064: Experimental Crystal Structure Determination, 2026, DOI: **10.5517/ccdc.csd.cc2pj14f**; (*c*) CCDC 2488065: Experimental Crystal Structure Determination, 2026, DOI: **10.5517/ccdc.csd.cc2pj15g**; (*d*) CCDC 2488066: Experimental Crystal Structure Determination, 2026, DOI: **10.5517/ccdc.csd.cc2pj16h**.

28 C. Zhu, G. Xu, D. Ding, L. Qiu and J. Sun, Copper-Catalyzed Diazo Cross-/Homo-Coupling toward Tetrasubstituted Olefins and Applications on the Synthesis of Maleimide Derivatives, *Org. Lett.*, 2015, **17**, 4244–4247.

29 K. W. Ace, N. Hussain, D. C. Lathbury and D. O. Morgan, Synthesis of an a-(Aminooxy)arylacetic Ester by the Reaction of an α-Diazo Ester with N-Hydroxyphthalimide, *Tetrahedron Lett.*, 1995, **36**, 8141–8144.

30 C. Xu, Y. Wang and L. Bai, Copper(I)-Catalyzed Aerobic Oxidation of α-Diazoesters, *J. Org. Chem.*, 2020, **85**, 12579–12584.

31 M. J. Mailloux, G. S. Fleming, S. S. Kumta and A. B. Beeler, Unified Synthesis of Azepines by Visible-Light-Mediated Dearomative Ring Expansion of Aromatic N-Ylides, *Org. Lett.*, 2021, **23**, 525–529.

32 Y. Ben-Tal and G. C. Lloyd-Jones, Kinetics of a Ni/Ir-Photocatalyzed Coupling of ArBr with RBr: Intermediacy of ArNiII(L)Br and Rate/Selectivity Factors, *J. Am. Chem. Soc.*, 2022, **144**, 15372–15382.

33 Y. Ben-Tal, P. J. Boaler, H. J. A. Dale, R. E. Dooley, N. A. Fohn, Y. Gao, A. García-Domínguez, K. M. Grant, A. M. R. Hall, H. L. D. Hayes, M. M. Kucharski, R. Wei and G. C. Lloyd-Jones, Mechanistic analysis by NMR spectroscopy: A users guide, *Prog. Nucl. Magn. Reson. Spectrosc.*, 2022, **129**, 28–106.

